Advances in Water Resources 114 (2018) 236–248

Contents lists available at ScienceDirect

Advances in Water Resources

journal homepage: www.elsevier.com/locate/advwatres

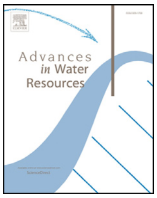

Modeling the poroelastic response to megathrust earthquakes: A look at the 2012 M_w 7.6 Costa Rican event

Kimberly A. McCormack[a,*], Marc A. Hesse[a,b]

[a] Department of Geosciences, University of Texas at Austin, Austin, TX, USA
[b] Institute for Computational Engineering and Science, University of Texas at Austin, TX, USA

ARTICLE INFO

Article history:
Received 24 July 2017
Revised 9 February 2018
Accepted 14 February 2018
Available online 21 February 2018

ABSTRACT

We model the subsurface hydrologic response to the 7.6 M_w subduction zone earthquake that occurred on the plate interface beneath the Nicoya peninsula in Costa Rica on September 5, 2012. The regional-scale poroelastic model of the overlying plate integrates seismologic, geodetic and hydrologic data sets to predict the post-seismic poroelastic response. A representative two-dimensional model shows that thrust earthquakes with a slip width less than a third of their depth produce complex multi-lobed pressure perturbations in the shallow subsurface. This leads to multiple poroelastic relaxation timescales that may overlap with the longer viscoelastic timescales. In the three-dimensional model, the complex slip distribution of 2012 Nicoya event and its small width to depth ratio lead to a pore pressure distribution comprising multiple trench parallel ridges of high and low pressure. This leads to complex groundwater flow patterns, non-monotonic variations in predicted well water levels, and poroelastic relaxation on multiple time scales. The model also predicts significant tectonically driven submarine groundwater discharge off-shore. In the weeks following the earthquake, the predicted net submarine groundwater discharge in the study area increases, creating a 100 fold increase in net discharge relative to topography-driven flow over the first 30 days. Our model suggests the hydrological response on land is more complex than typically acknowledged in tectonic studies. This may complicate the interpretation of transient post-seismic surface deformations. Combined tectonic-hydrological observation networks have the potential to reduce such ambiguities.

1. Introduction

1.1. Hydrologic effects of earthquakes

Earthquakes have long been known to produce a range of hydrological effects from short term responses such as liquefaction and eruption of mud volcanoes to long term changes in ground and surface water geochemistry, temperature and pressure (Manga and Wang, 2007; Miller, 2012; Wang and Chia, 2008; Wang and Manga, 2010). In the near field, within a few rupture lengths of the earthquake, the hydrological effects are due to both static and dynamic stress changes, while only dynamic stress changes can induce hydrologic responses over greater distances (Brodsky, 2003; Rojstaczer et al., 1995).

Here we are interested in the hydrologic response to subduction zone earthquakes. Given their large rupture zones, static stress changes extend over hundreds of kilometers. The co-seismic subsurface hydrologic response in the near field is often well correlated with the static poroelastic stresses (Akita and Matsumoto, 2004; Quilty and Roeloffs, 1997; Shi et al., 2013; Wakita, 1975). Near field post-seismic transients in pore pressure, surface deformation and fluid flux, consistent with poroelastic behavior, have been observed in various settings (Fialko, 2004; Jonsson et al., 2003; Labonte et al., 2009; Peltzer et al., 1998). These observations suggest that the regional groundwater flow induced by quasi-static stress changes is an important component of the hydrologic response to large subduction zone earthquakes.

While the complex effects of earthquakes on ground and surface water have received considerable attention (Mohr et al., 2016; Shi et al., 2015), much less is known about the potential submarine groundwater discharge (SGD) associated with tectonic stresses. This expulsion of fluids through the seafloor is expected from previous modeling studies given the compression of the forearc during subduction and due to thrust faulting events (Zhou and Burbey, 2014). Such tectonic fluxes have been observed along the Costa Rica margin subduction zone due to compaction of pelagic

---

[*] Corresponding author.
E-mail addresses: kimberly.mccormack@utexas.edu (K.A. McCormack), mhesse@jsg.utexas.edu (M.A. Hesse).

https://doi.org/10.1016/j.advwatres.2018.02.014

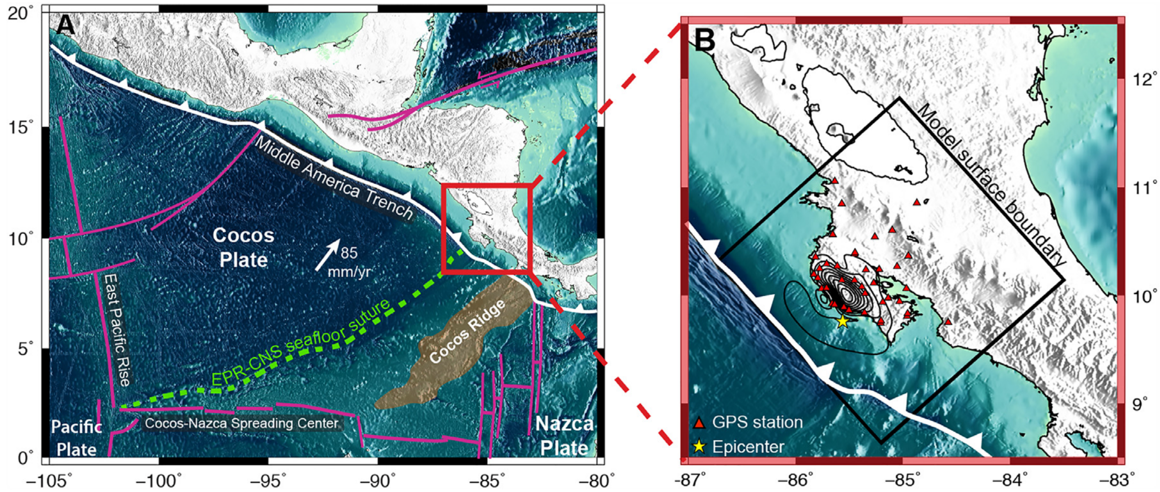

Fig. 1. Maps of the study area. a) Regional map illustrating the tectonic setting of the Middle America Trench (MAT) (modified from Feng et al. (2012)). b) Local map of the Nicoya Peninsula showing the GPS stations, epicenter (star) and slip magnitude contours (black lines with a 0.25 m contour interval) of the 2012 M_w 7.6 earthquake. The surface of the 3D model domain is indicated by the black box.

sediments on the down-going plate and compression from slow slip events near the trench (Labonte et al., 2009; Screaton and Saffer, 2005). These SGDs occur in deep water close to the subduction trench.

Shallow SGD near the coast has also been studied, primarily due to its effect on the chemistry of the coastal ocean (Moore, 1996; Slomp and Van Cappellen, 2004). This type of SGD derives in part from topography driven flow in aquifers that drain directly to the coast and are expelled close the shoreline (Sawyer et al., 2016). As part of this study, we investigate the possible impact of a large earthquake on the location and magnitude of SGD. We use fully coupled poroelastic models to study tectonic driven SGD for a large subduction zone earthquake in Costa Rica that occurred beneath the Nicoya peninsula in 2012.

We have chosen this event because of the unique location of the Nicoya peninsula above the slipping portion of the subduction zone interface. This together with a dense network of high rate Global Positioning System (GPS) stations provides excellent constraints on the co-seismic deformation driving the groundwater flow. However, due to the absence of transient hydrological monitoring it is not possible to validate the predicted hydrologic response.

The aim of this manuscript is therefore to investigate the basic features of the large-scale poroelastic relaxation following the 2012 Costa Rica earthquake. To determine the significance of the tectonically driven groundwater flow we compare it to the standard model of topography driven flow. Both models have identical material properties and geometry, but have different boundary conditions. Discussing the tectonic flow relative to the topographic flow mitigates the effect of highly uncertain parameter values, such as the permeability.

1.2. Costa Rica and the 2012 $\mathrm{M_w}$ *7.6 earthquake*

Along the Pacific coast of Costa Rica, the oceanic Cocos Plate derived from the East Pacific Rise and Cocos-Nazca Spreading center subducts along the Middle America Trench (MAT) with a velocity of 8.5–9 cm/yr (DeMets et al., 2010; Feng et al., 2012), as shown in Fig. 1*a*. The resulting volcanic arc extends from central Costa Rica north into Mexico. In the south, the MAT extends to the Panama Fracture Zone, a transform fault separating the Cocos and Nazca oceanic plates. The suture within the Cocos plate subducts directly beneath the Nicoya peninsula. On the northern side of this suture zone, smoother, older oceanic crust (25–30 Ma) derived from the East Pacific Rise is being subducted. On the southern side, slightly younger sea floor derived from the Cocos–Nazca Spreading Center subducts underneath Costa Rica (DeShon et al., 2006).

On September 5, 2012, a magnitude 7.6 earthquake ruptured the plate interface beneath the Nicoya Peninsula, Costa Rica. The epicenter was located 12 km offshore from the central Nicoya coast, at a depth of approximately 18 km (Fig. 1*b*). The rupture spread outward along the plate interface to encompass 3000 km^2 of the Nicoya seismogenic zone (Yue et al., 2013). The Nicoya Peninsula is positioned over the seismogenic zone of the subduction plate interface. Thus, surface deformation measurements provide reliable information about deformation on the slab interface. Fig. 1*b* shows contours of the slip estimated from a combination of 21 campaign GPS stations and 18 continuous stations deployed on the Nicoya Peninsula (Protti et al., 2013).

2. Model setup

2.1. Governing equations and boundary conditions

To model the instantaneous and time-dependent poroelastic response to the earthquake, we use a fully coupled, linear poroelastic model. The slip distribution of the earthquake on the fault plane is applied as a boundary condition (Yue et al., 2013), which initializes the co-seismic pressures and displacements. This instantaneous undrained response evolves as the pore pressure equilibrates.

The linear poroelastic theory developed by Biot provides a system of equations that describes the coupling between the flow of pore fluids and the deformation of the rock matrix (Wang, 2000). The governing equations, combining the conservation of fluid mass for the evolution of pore fluid pressure, $p = p(\mathbf{x}, t)$, and total momentum conservation of the porous medium for the quasi-static solid displacement, $\mathbf{u} = \mathbf{u}(\mathbf{x}, t)$, in a domain, Ω, over the time interval, [0, *T*], are given by

$$(S_\epsilon p + \alpha \nabla \cdot \boldsymbol{u})_t - \nabla \cdot \left(\frac{\kappa}{\mu} \nabla p \right) = 0 \qquad \text{in}\, \Omega, \tag{1a}$$

$$-\nabla \cdot (\boldsymbol{\sigma}(\boldsymbol{u}) - \alpha p \boldsymbol{I}) = 0 \qquad \text{in}\ \Omega, \tag{1b}$$

where $(\cdot)_t$ denotes the time derivative, S_ϵ is the specific storage, $\kappa(\mathbf{x})$ is the permeability, μ is the fluid viscosity and α is the Biot–

Willis parameter. In an elastic medium, the stress tensor, $\boldsymbol{\sigma}$, is related to displacement as follows:

$$\boldsymbol{\sigma}(\boldsymbol{u}) = G\left(\nabla \boldsymbol{u} + \nabla \boldsymbol{u}^T\right) + G\frac{2\nu}{1-2\nu}(\nabla \cdot \boldsymbol{u}) \tag{2}$$

where G and ν are the elastic shear modulus and drained Poisson's ratio, respectively.

The Biot–Willis parameter, α and the specific storage coefficient, S_ϵ can be written in terms of the elastic parameters as

$$\alpha = \frac{3(\nu_u - \nu)}{B(1+\nu_u)(1-2\nu)}, \quad S_\epsilon = \frac{3\alpha(1-2\nu)(1-\alpha B)}{2GB(1+\nu)}$$

where B is Skempton's pore pressure coefficient and ν and ν_u are the drained and undrained Poisson's ratios, respectively. The poroelastic Eq. (1) require four independent material parameters to describe the undrained response as well as the magnitude of the relaxation: ν, ν_u, G and B, representing the drained Poisson's ratio, the undrained Poisson's ratio, the elastic shear modulus and Skempton's coefficient, respectively. Two additionally parameters, κ and μ control the transient behavior of the pore fluid.

The models for the poroelastic response to an earthquake and topographic-driven flow have different sets of boundary conditions. The primary difference between the earthquake-driven and topographic-driven models is the pressure boundary condition on the land surface. In the case of the earthquake-driven flow, the boundary representing the land surface is set as a no flow boundary condition, the limitations of which are discussed in Section 4.2. For the topographic flow model, the land surface boundary is set with a spatially-varying pressure field equal to a smooth, subdued expression of the land surface representing the water table. The boundary and initial conditions for the earthquake-driven model are:

$$p(\cdot,0), u(\cdot,0) = 0 \quad \text{in } \Omega \tag{3a}$$

$$p = 0 \quad \text{on } \Gamma_{ocean} \tag{3b}$$

$$(\kappa/\mu \nabla p) \cdot \boldsymbol{n} = 0 \quad \text{on } \Gamma_{notocean} \tag{3c}$$

$$\boldsymbol{\sigma}(\boldsymbol{u})\boldsymbol{n} = 0 \quad \text{on } \Gamma_{surface} \tag{3d}$$

$$\boldsymbol{u} \cdot \boldsymbol{n} = 0 \quad \text{on } \Gamma_{right}, \Gamma_{bottom} \tag{3e}$$

$$\boldsymbol{u} \cdot \boldsymbol{n} = 0 \quad \text{on } \Gamma_{slab} \tag{3f}$$

$$\delta\boldsymbol{\sigma}(\boldsymbol{u})\boldsymbol{n} \cdot \boldsymbol{t} + \boldsymbol{u} \cdot \boldsymbol{t} = \boldsymbol{u}_0 \quad \text{on } \Gamma_{slab} \tag{3g}$$

For the case of topographic driven flow, the initial and boundary conditions are:

$$p(\cdot,0), u(\cdot,0) = 0 \quad \text{in } \Omega \tag{4a}$$

$$p = 0 \quad \text{on } \Gamma_{ocean} \tag{4b}$$

$$p = p_{topo} \quad \text{on } \Gamma_{land} \tag{4c}$$

$$(\kappa/\mu \nabla p) \cdot \boldsymbol{n} = 0 \quad \text{on } \Gamma_{notsurface} \tag{4d}$$

$$\boldsymbol{\sigma}(\boldsymbol{u})\boldsymbol{n} = 0 \quad \text{on } \Gamma_{surface} \tag{4e}$$

$$\boldsymbol{u} \cdot \boldsymbol{n} = 0 \quad \text{on } \Gamma_{right}, \Gamma_{bottom} \tag{4f}$$

$$\boldsymbol{u} = 0 \quad \text{on } \Gamma_{slab} \tag{4g}$$

In both cases, the overlying ocean applies a hydrostatic pressure at the seafloor, which results in a zero pressure boundary condition, as p represents the deviation of the pressure from hydrostatic. Our model ignores the effects of tides on the ocean bottom pressure due to the much shorter spatial and temporal scales on which tide-induced pressure signals propagate into the seabed. All other boundaries, including the one representing the land surface, are set as no flow boundaries.

The normal stress on both the ocean and the land surface is set to zero to allow for surface deformation. On the slab interface the displacement is assumed to be only in the tangential directions and is prescribed by the inversion of geodetic data, the magnitude of which is shown in Fig. 1b. The vertical boundary opposite of the trench and the bottom boundary are set as roller boundaries to prevent a net rotation of the domain. The mathematical formulation of these boundary conditions is given in Appendix 1.

2.2. Model geometry

The three-dimensional (3D) model surface comprises an area of 250 km by 250 km aligned with the trench and extending into the overriding continental plate. The location of the model is shown on the map in Fig. 1a. All locations and displacements are rotated into a trench perpendicular and trench parallel coordinate system. The 3D model geometry in shown in Fig. 2a and the trench perpendicular cross-section used for the two-dimensional (2D) model is shown in Fig. 2b.

A simplified coastline is integrated into the mesh and divides the top boundary of the domain into two surfaces. The seafloor is defined as a linear slope from the coast at 0 km depth to the trench at 4 km depth, while the land topography is neglected. The fault interface boundary of the model is fit to the smooth interface derived from seismic tomography and is assumed constant in the trench-parallel direction (DeShon et al., 2006). The model domain is truncated at 60 km depth.

In both 2D and 3D, it is necessary to resolve the near surface such that the permeability decay with depth (Fig. 3A) is adequately captured by the mesh. In 2D, this can be done with an unstructured tetrahedral mesh with an element size of 200 m at the surface and 3 km at depth, resulting in approximately 60,000 elements. In 3D, this is done with an extruded, layered mesh from 0–5 km depth - comprising of 4 layers that increase in thickness with depth from 300 to 1,500 m - overlaying an unstructured tetrahedral mesh with 3–4 km element size. This allows the model to capture the permeability decay without meshing to a 300 m resolution in the x and y directions. The 3D mesh contains approximately 140,000 elements. We use a direct solver and only rebuild the factorization when the timestep changes. To efficiently capture both rapid short-term and slow long-term behavior, the timestep progresses from 15 min to one month. All of the models were run on a workstation with run times ranging from 1 to 30 h. The limitation on the number of elements used is the memory required to store the factorization.

2.3. Integration of field data

The six parameters of the poroelastic model described above vary both laterally and with depth, and potentially over many orders of magnitude. They should therefore ideally be constrained by field data. Below we describe how parameter values throughout

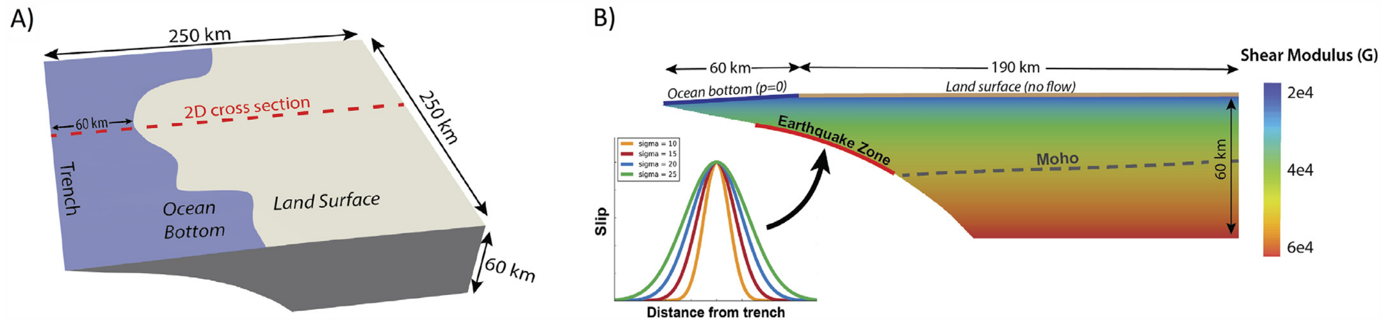

Fig. 2. Geometry of the 2D and 3D model. A) 3D model geometry with the boundary between the land and ocean surface as well as the location of the 2D cross section shown. B) 2D model with the shear modulus (G) distribution and the location and slip of imposed earthquakes along the fault boundary.

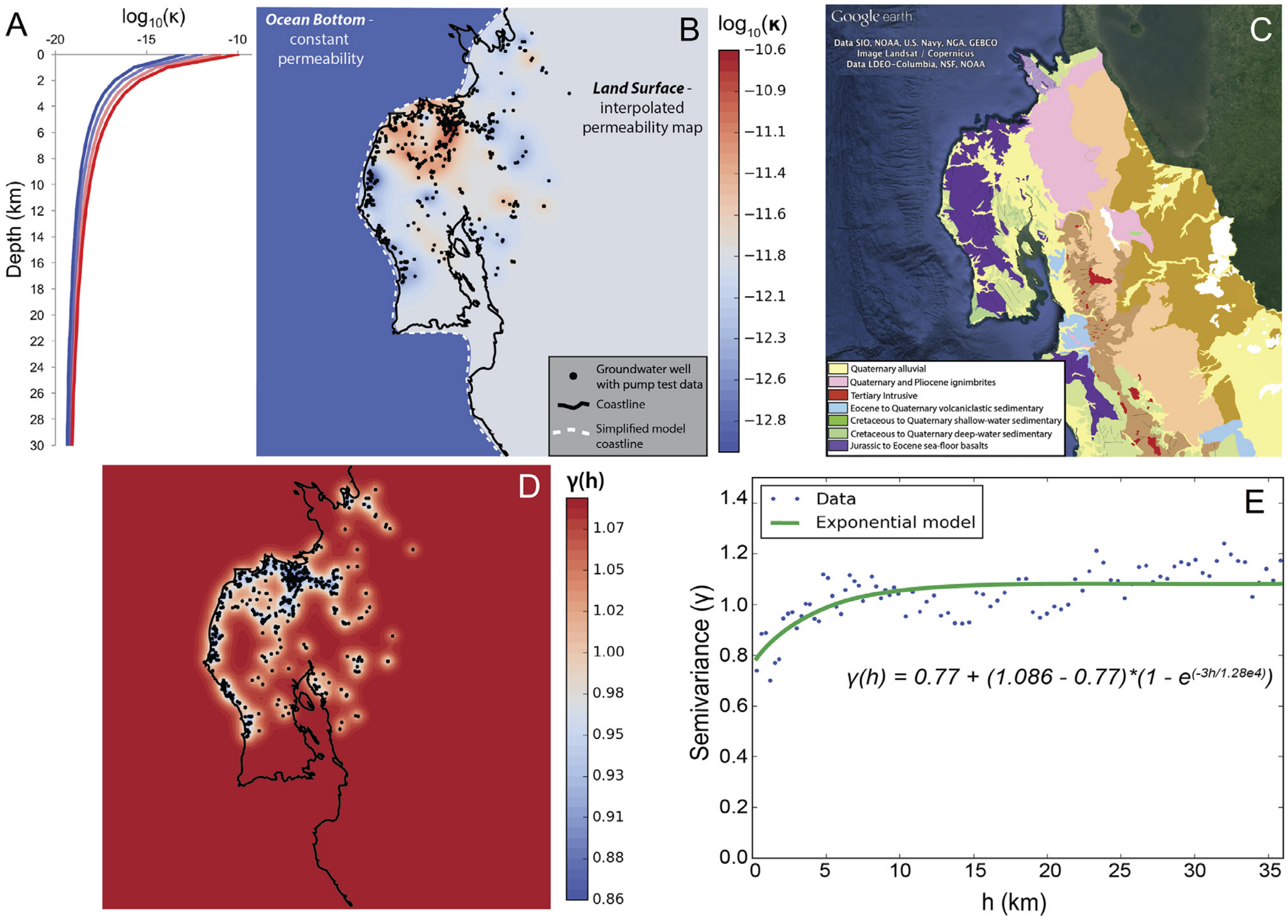

Fig. 3. Permeability interpolation. A) Permeability decay with depth for the range of surface permeability values. B) Spatially interpolated near-surface permeability map. C) Geologic map of the study area obtained from the U.S. Geological Survey (Schruben, 1996). D) Spatial distribution of variance of the estimated permeability field. E) Semivariogram of the permeability in the study area.

the domain have been derived from regional seismic and hydrogeologic data.

2.3.1. Elastic parameters and initial slip condition

It is increasingly recognized that the spatial variation of the elastic parameters has a significant influence on the predicted coseismic displacements (Masterlark et al., 2001; Williams and Wallace, 2015). The elastic parameters of the model are constrained with V_p/V_s seismic tomography data along with a 1D density model to create best fit functions that represent how the various elastic parameters change with depth (DeShon, 2004; DeShon et al., 2006). Fig. 2b shows how the tomography-derived shear modulus, G, varies within the domain.

The Young's modulus is calculated from P-wave velocity and density. The P-wave velocity, V_p, and the bulk density, ρ_b, depth profile are used to calculate the P-wave modulus, M, with depth using $M = \rho_b V_p^2$. The P-wave modulus and drained Poisson's ratio, ν, are then used to derive the Young's modulus, E, depth profile using the relationship: $E = M(1+\nu)(1-2\nu)/(1-\nu)$. Three parameters for a power function of the form, $E(z) = az^b + c$, were fit to the relationship between Young's modulus and depth, resulting in a best fit function of $E = 3.471z \cdot 10^2\ ^{.0.5157} + 5.324 \cdot 10^4$, where z is the depth in meters and E is given in MPa. The shear modulus, G, used in the poroelastic equations, is derived from Young's modulus and Poisson's ratio using the relationship: $G = E/(2(1+\nu))$.

The slip boundary condition to drive the model is obtained by inverting the co-seismic displacements measured by a network of GPS stations. Here we use the co-seismic displacements to infer slip on the overridding plate of the subduction interface. The contour map of the slip solution is shown in Fig. 1b. The co-seismic horizontal surface displacement vectors at GPS station locations from both GPS measurements and the forward model are shown in appendix figure Fig. A.1.

2.3.2. Hydrogeologic data

The timescale over which fluid-induced deformation takes place is controlled by the three dimensional permeability field. Our model considers the variations in permeability that occur on two different length scales. A general decline of permeability with depth on the crustal scale and large variations that occur over short lateral distances in the relatively permeable shallow crust.

On the crustal scale, the permeability, κ, decreases exponentially with depth, $d = -z$, from the high permeability, κ_s, near the surface to the low residual background permeability lower in the crust, κ_r, as shown in Fig. 3a. We use the parameterization of Kuang and Jiao (2014), given by

$$\log_{10}(\kappa) = \log_{10}(\kappa_r) + \log_{10}\left(\frac{\kappa_s}{\kappa_r}\right)(1-d)^{-a} \tag{5}$$

where $a = 0.8$ is the dimensionless decay index. We assume that κ_r is constant, but allow κ_s to vary laterally, as shown in Fig. 3b.

To constrain the surface permeability field, κ_s, of the study area, we obtained pump test results of 520 groundwater wells from SENARA, located throughout the state of Guanacaste, Costa Rica, see SI. The pump test results were interpreted in terms of the transmissivity of the aquifer, T. If the aquifer thickness, b, is known, the hydraulic conductivity is given by $K = T/b$. Here we assume that b is equal to the reported well depth. This assumption tends to overestimate K if the well does not penetrate the entire depth of the aquifer. The permeability required for (1a), is given by $\kappa = K\mu/(\rho g)$, where ρ is the density of the pore fluid and g is the acceleration of gravity. The permeabilites obtained this way should be seen as upper bound, because of our assumption that the wells penetrate the entire aquifer.

The well data were interpolated using a kriging toolbox (Murphy, 2014). In areas on land not covered by the well data the permeability reverts to the mean permeability of the well data set. In absence of data about the spatial variation of seafloor permeability we assume it is constant and choose a value of 10^{-13} m^2 based on previous studies (Becker and Davis, 2004; Davis and Villinger, 2006; Spinelli et al., 2004). The resulting permeability map is shown in Fig. 3b. The northwest and central portions of the Nicoya Peninsula have generally higher surface permeabilities whereas the southern and inland portions have much lower permeability. Comparison with the geological map in Fig. 3c shows that high permeability areas often associated with Quaternary alluvial sediments while low permeability areas are primarily sea-floor basalts.

The kriging variance in Fig. 3d shows that the permeability is highly uncertain away from the well data. This is due to the short correlation length of the data, evident from the semivariogram of the data in Fig. 3e. For the kriging interpolation we have assumed an exponential variogram model with a nugget, sill and range of 0.771, 1.086, and $1.28{\cdot}10^4$ m, respectively.

There is currently no well monitoring system in place of the Nicoya peninsula. Therefore, no quantitative records of the head changes during and after the earthquake exist. However, qualitative description of the response at an individual location has been reported and is discussed below.

3. Results

For this study we used both 2D and 3D numerical models. In Section 3.1 we investigate more general trends in the poroelastic response in a 2D model of a subduction zone earthquake given different earthquake sizes and crustal permeability structures. Section 3.2 presents results of a 3D model results based on a fixed set of best fit parameters and the real earthquake slip data.

3.1. Two-dimensional model results

In order to gain a better understanding for which factors control both the co-seismic and post-seismic poroelastic response to a large earthquake, we ran a number of simpler models in 2D. The geometry is based on a representative trench-perpendicular cross-section through the center of the Nicoya peninsula and the slip patch (Fig. 2). These models use a constant surface permeability, but retain the variation of permeability and Young's modulus with depth. First we discuss the geometry of the co-seismic undrained elastic response in Section 3.1.1, followed by a discussion of the time-scales of the post-seismic poroelastic relaxation in Section 3.1.2.

3.1.1. Effects of earthquake size and depth on the undrained response

To study the 2D instantaneous response to a subduction zone earthquake we use a synthetic Gaussian slip distribution. For a Gaussian slip centered at a depth of 20 km with a rupture width of 100 km, the co-seismic displacement and the undrained pore pressure response are shown in Fig. 4a and b, respectively. For a Gaussian slip distribution, the rupture width is defined as $4\sigma_{slip}$, where σ_{slip} is the variance of the Gaussian function. The simulation shows the expected increase in pore pressure due to compression of the forearc and decrease due to extension in the interior. This simple pattern is observed when the width of the slip patch is large relative to the earthquake depth. In this case, pore pressure increases trenchward of the earthquake - primarily offshore - and decreases behind the earthquake on land.

However, earthquakes with a smaller slip area relative to their depth produce a more complex pattern in co-seismic displacement and the undrained pore pressure response (Fig. 4c and d). In the far-field, the pattern is similar, but directly above the earthquake two additional pressure lobes appear near the surface. A similar pattern of the instantaneous pore pressure field, in response to a thrust earthquake, was described in Zhou and Burbey (2014). Fig. 5 shows that the undrained pore pressure pattern is primarily a function of the ratio of slip extent to earthquake depth. The four-lobed pattern is observed when the slip width to depth ratio is equal to or less than three. The elastic parameters have a very small effect on this geometry, but if the Young's modulus increases drastically with depth the pattern trends toward the simple two lobed case.

This four lobed pattern is conspicuous in the pore pressure response, but is less obvious in the surface displacement. Fig. 6 shows that the local pore pressure maximum is accompanied by some subsidence and a decrease in the magnitude of the trenchward displacement. The local decrease in the amount of trenchward displacement results in an area directly above the earthquake that experiences less net displacement, which results in local landward compression and trenchward expansion. For earthquakes with small slip width to depth ratios (Fig. 4c), these local high and low pressure lenses dominate the local near surface hydrologic response. Displacement data from the Nicoya peninsula projected onto the cross-section show a pattern consistent with four-lobed pressure response (Fig. 6).

The undrained pressure field sets up regional groundwater flows that relax the pressure gradients over time. The timescale of

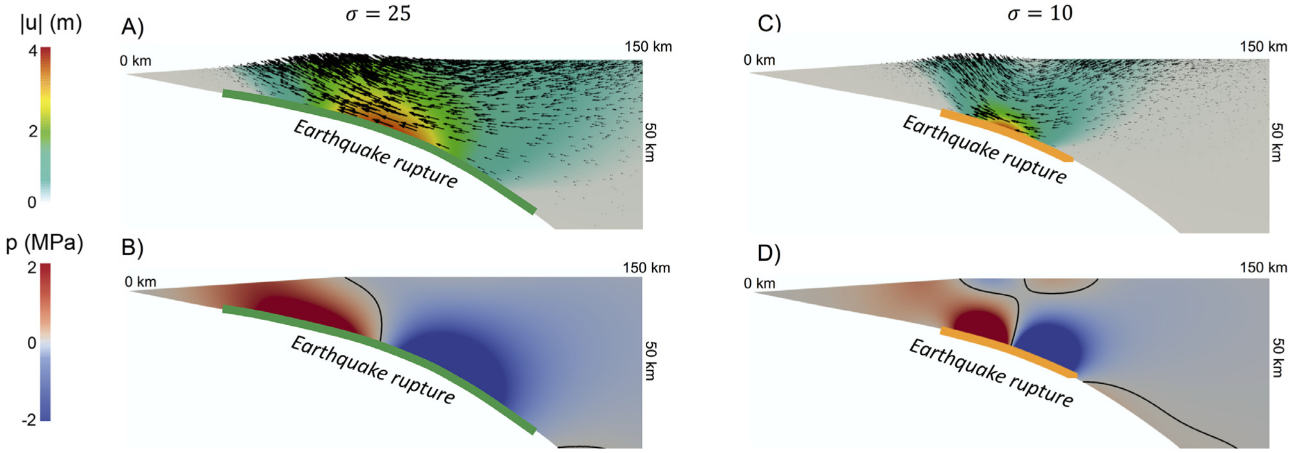

Fig. 4. Instantaneous, undrained response to an megathrust earthquake. A) Deformation magnitude and slip vectors for an imposed Gaussian slip distribution with a width to depth ratio of 5:1 along the earthquake rupture zone (green line). B) Instantaneous pore pressure response to earthquake in A. C) Deformation magnitude and slip vectors for an imposed Gaussian slip distribution with a width to depth ratio of 2:1 along the earthquake rupture zone (orange line). D) Instantaneous pressure response to an earthquake with a standard deviation of 10 km (C). (For interpretation of the references to colour in this figure legend, the reader is referred to the web version of this article.)

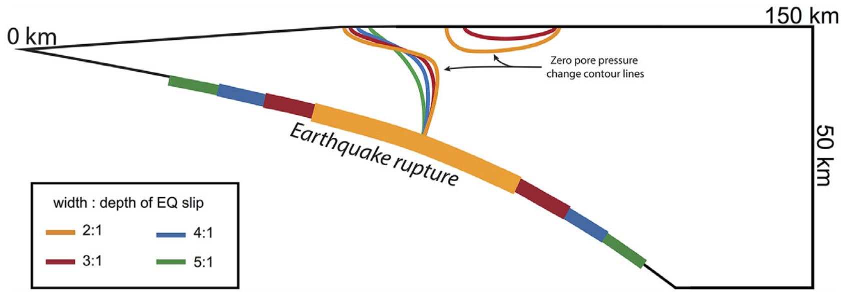

Fig. 5. Contour lines of zero pore pressure change and corresponding earthquake rupture length. As the rupture length of the earthquake decreases, while the depth remains the same, a high pressure lens is produced and the extent of the high pressure region in front of the earthquake is driven trenchward.

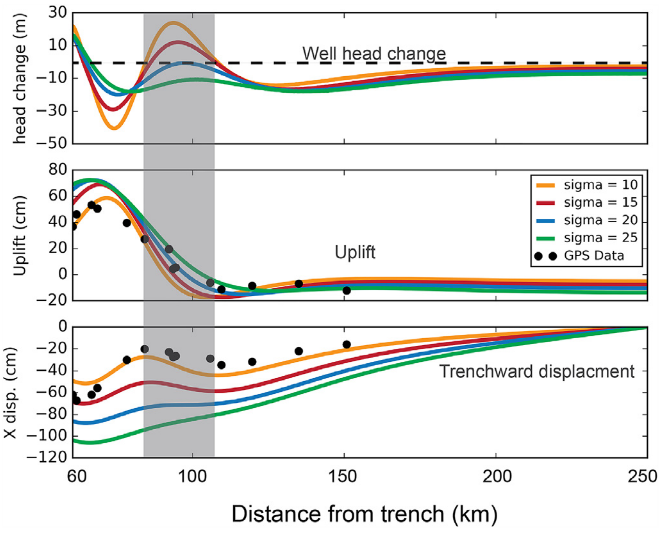

Fig. 6. Instantaneous near-surface water level change, uplift and trenchward displacement for earthquakes with different slip width to depth ratios. GPS displacements for stations within 20 km of the 2D transect are shown as black dots. Grey bar indicates region with a negative gradient of trenchward displacement, creating compression and corresponding to a positive near-surface pore pressure change.

the hydrological response is determined by the near surface permeability and mass specific storage. In the 2D model the permeability only varies with depth and remains constant across the surface. This allows us to look at the effect of different surface permeability values on the time-dependent pore pressure response without the added complication of large-scale preferential flow paths present in the 3D model.

To study the time dependent hydrological response we perform a 2D simulation with a slip distribution that is a Gaussian approximation of the 2012 Nicoya event, a surface permeability of 10^{-11} m^2 and a Skempton's coefficient of 0.7. The undrained pressure distribution and the transient well head, $h = p/\rho g$, response at various locations on the surface are shown in Fig. 7. The slip-width to depth ratio of the main slip patch of the 2012 Nicoya event is approximately 2:1 and hence results in a four-lobed instantaneous pore pressure response in the shallow crust.

3.1.2. Time-dependent hydrological response

The signature of the transient pore pressure relaxation after the earthquake varies significantly with distance from the trench (Fig. 7). The response differs from what might be expected, because the head response is complicated by the four-lobed pattern that leads to a local head maximum above earthquake. First, we will discuss the change in the well response with distance from the coast and then consider the effect of the near surface permeability.

Very close to the coast, Fig. 7a shows an instantaneous rise followed by, in most cases, a drop below pre-earthquake levels. Just two kilometers inland, Fig. 7b shows a co-seismic head drop, followed in most cases by a continued decrease, and then a recovery. In the low pressure regions close to the coast and far inland (Fig. 7c and f), an instantaneous head drop is followed by a monotonic recovery. In the center of the high pressure lens (Fig. 7d),

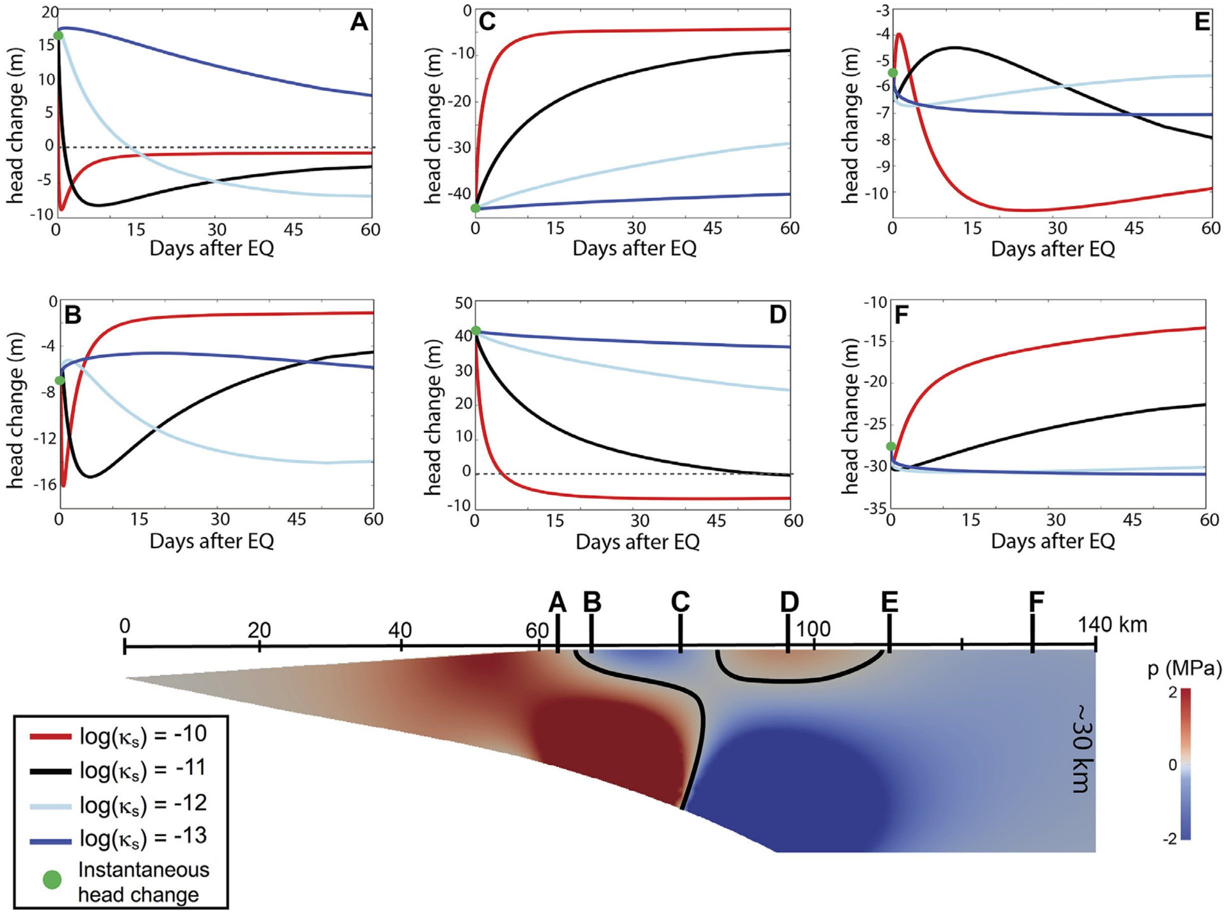

Fig. 7. Time-dependent pressure response along the surface of the 2D model. The instantaneous pressure for the entire domain is shown below modeled time-series of water level at points along the surface. Time series show the well head evolution for different values of near-surface permeability ranging from 10^{-10} to 10^{-13}. For the same initial pore pressure change, different permeability values lead to very different relaxation patterns.

an instantaneous head increase is followed by a monotonic relaxation to a head sometimes below the pre-earthquake level. The wells in the transition zones between high and low pressure regions show markedly different patterns of transient well response. Behind the high pressure lens, a co-seismic head drop is followed either by a recovery and drop or a small drop and recovery (Fig. 7e).

The initial well response is due to the dissipation of the four-lobed pressure pattern within the first twenty days. After the dissipation of the local pressure maximum above the earthquake, the entire onshore region is under-pressured compared to pre-earthquake pore pressures. This induces a slow landward regional groundwater flow from the overpressured section offshore. While well levels close to the coast recover quickly (Fig. 7a), the recovery further inland (Fig. 7f) may take months to years.

Fig. 7 also illustrates the effect of variations in surface permeability on the transient well head response. Fig. 7c shows the expected delay in recovery with decreasing permeability. However, Fig. 7e shows that variations in permeability can also lead to fundamental changes in the pattern of well head response. This particular well changes from a non-monotonic head response to a monotonically decreasing response as the permeability decreases. Both panels illustrate that the instantaneous response is independent of permeability.

3.1.3. Submarine groundwater discharge (SGD)

The offshore compression due to the earthquake leads to the expulsion of significant amounts of pore water through the seafloor. It is interesting to compare this discharge to continuous SGD driven by topography and compression by subduction.

Topography driven flow assumes that the water table is a subdued expression of the surface topography (Cherry and Freeze, 1979; Toth, 1962), and provides a simple estimate for the shallow environmental flows in the hydrological cycle (Gleeson et al., 2015; Sawyer et al., 2016). An estimate of the topography driven SGD is shown in Fig. 8a. The representative cross section through the Nicoya Peninsula shows two mountain ranges separated by a central valley. The elevated pressures underlying the topographic highs induce flows down-gradient into the valleys and out to sea. The insert of Fig. 8a shows the details of the flow field near the surface. The streamlines illustrate that groundwater flow occurs in is confined to the upper most 500 m. The SGD due to this shallow topography driven flow is therefore localized in the first few hundred meters off the coast. Assuming the water table varies between 25 and 75% of the land surface topography, the total SGD per unit width is between 2000–6000 $\text{m}^3/(\text{m yr})$. Additionally, subduction of the oceanic plate compresses the toe of the overriding plate and produces SGD on the order of 100 $\text{m}^3/(\text{m yr})$, primarily near the trench.

The pattern of tectonic-driven SGD differs significantly from the topography-driven SGD. Following an earthquake, compression offshore leads to SGD along most of the seafloor between the coast and the trench (Fig. 8b). Unlike the topographic flow, which induces mostly horizontal flow, the tectonic-driven flow is mostly vertical. The total flux through the seafloor immediately following the earthquake is four orders of magnitude greater than the

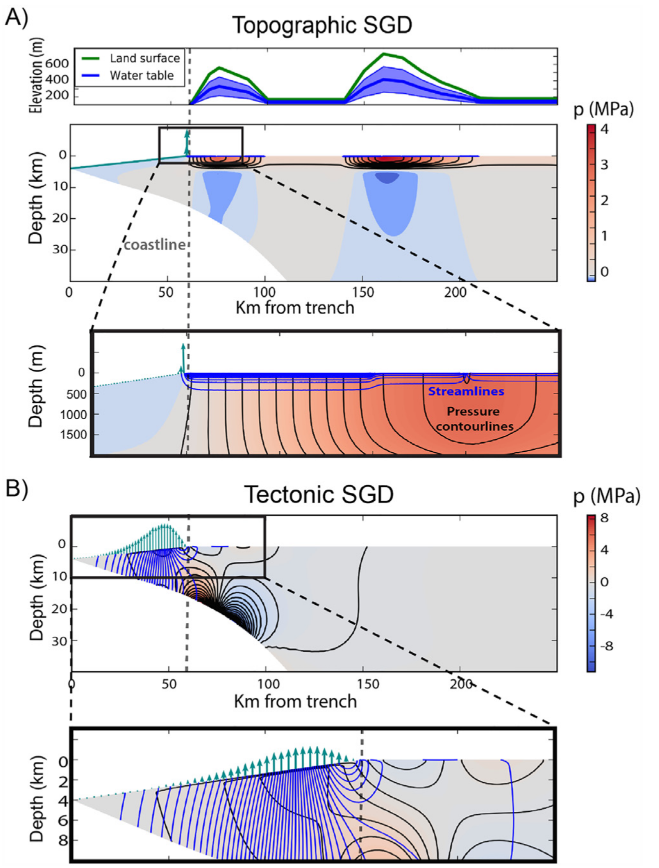

Fig. 8. Topography-driven and tectonic driven submarine groundwater discharge. A) steady-state flow net for 2D topography driven flow given the topographic cross section of the Nicoya Peninsula (shown above). The lower figure shows almost all of the flow occurs in is confined to the top 500 m and flows out through the sea floor within a few hundred meters of the coastline. The light blue arrows represent linear flow velocities. B) Pore pressure change and streamlines immediately following an earthquake. In this case, the groundwater is expelled at a much higher rate (arrows do not scale with flux between figures) and over a much larger region, with the maximum flux occurring well offshore. (For interpretation of the references to colour in this figure legend, the reader is referred to the web version of this article.)

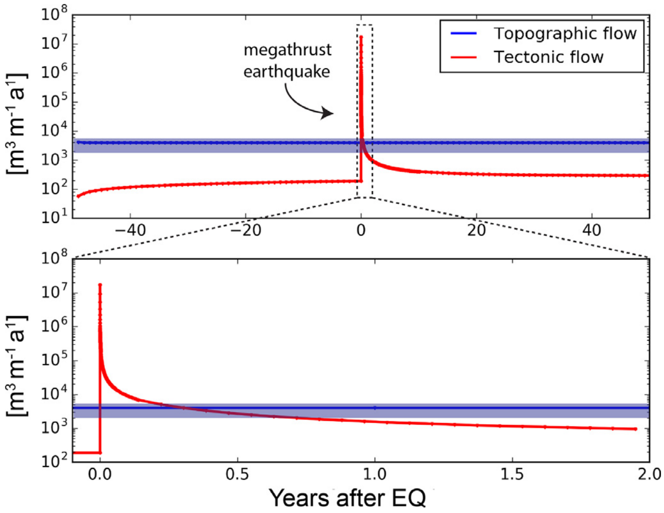

Fig. 9. Comparison of the total SGD produced by topography and tectonic-driven flow in 2D. Subduction of the ocean plate produces SGD much lower than topographic flow. An earthquake produces a spike in simulated SGD followed by a multi-year decline to a new base level of subduction-driven SGD.

topographic flux (Fig. 9). The tectonic contribution to SGD remains greater than the topographic contribution for approximately 3 months following the earthquake, and remains elevated for a number of years.

The tectonically driven SGD due to smaller events, such as slow slip events, have been previously detected by fluid flux measurements offshore the Nicoya Peninsula (Jiang et al., 2017; Labonte et al., 2009). Our simulations show that that large events are likely to induce similar flows that significantly change the pattern and magnitude of SGD in the months following an earthquake.

3.2. Three-dimensional model results

The two-dimensional results presented above are instructive, but they lack the complex slip distribution of the earthquake and the spatial heterogeneity of permeability in the upper crust. To address these effects, we conduct a three dimensional simulation, incorporating all of the available data to constrain the earthquake geometry and poroelastic parameters. Whereas the 2D model was used to investigate the effects of different parameters on the instantaneous and time-dependent responses, the 3D model uses a single set of best fit parameters for the Nicoya Peninsula and the 2012 earthquake. Table 1 summarizes the model parameters and the data used to constrain them. Unlike the 2D model, where the slip distribution was assumed to be Gaussian, the 3D model incorporates the realistic slip distribution shown in Fig. 1b.

The most prominent feature of the instantaneous hydrologic response are the trench parallel ridges of high and low head in the shallow subsurface (Fig. 10a). There are two possible reasons for this pattern: 1) the width to depth ratio of the main slip region or 2) the horseshoe pattern of the slip distribution. The pattern of high and low head changes on land occurs directly over the main slip patch of the earthquake. The secondary slip area near the trench is too far away to affect the onshore, subsurface head response. The width of the main slip patch of the Nicoya earthquake is 40 km (Fig. 1b) and the depth of the epicenter is 18 km. The slip width to depth ratio is therefore less than 3:1, suggesting that this multi-lobed head response in Fig. 10a–d is the 3D manifestation of the modeled 2D response for earthquakes with small slip width to depth ratios (Fig. 4c,d).

While no formal well monitoring system is in place on the Nicoya peninsula, a well located at 10.06333N, 85.26055W overflowed for several minutes during and after the earthquake in an area that subsided during the event (Protti, 2015). This well lies behind the earthquake slip in an area that would be expected to exhibit a head drop after the earthquake. However, the 3D model predicts compression and an increase in well level at this location, and is therefore consistent with this observation. Inelastic consolidation processes due to dynamic stresses are also commonly observed to induce increases in well levels.

The transient head responses in 3D at different locations in the shallow subsurface show many of the same features that are seen in the 2D model. Areas within the regional extrema exhibit generally monotonic behavior, while locations in the transition zones between these extrema often undergo non-monotonic transient head responses (Fig. 10f,h). Pressure dissipation in 3D, like in 2D, occurs over multiple timescales. The local pressure maximum in Fig. 10g largely dissipates within 60 days while the regional pressure drop located mostly in a lower permeability region (Fig. 10e) requires up to 3 years to recover. These timescales are affected by the permeability heterogeneity in the near surface. For example, lateral permeability variations result in the rapid dissipation of the high pressure region in the northwest of the Nicoya peninsula versus the slower decline of the local pressure maximum in the center of

Table 1
Table of chosen and interpolated parameter values for both 2D and 3D numerical models .

Parameter	2D	3D	ref.
G [MPa]	$2-6\cdot10^4$	$2-6\cdot10^4$	DeShon et al. (2006)
ν	0.27	0.27	
ν_u	0.38	0.38	
B	0.6	0.6	
κ_s [m^2]	$10^{-(10-13)}$	Fig. 3	SENARA (0000), Becker and Davis (2004), Spinelli et al. (2004) and Davis and Villinger (2006)
μ [MPa·s]	10^{-9}	10^{-9}	

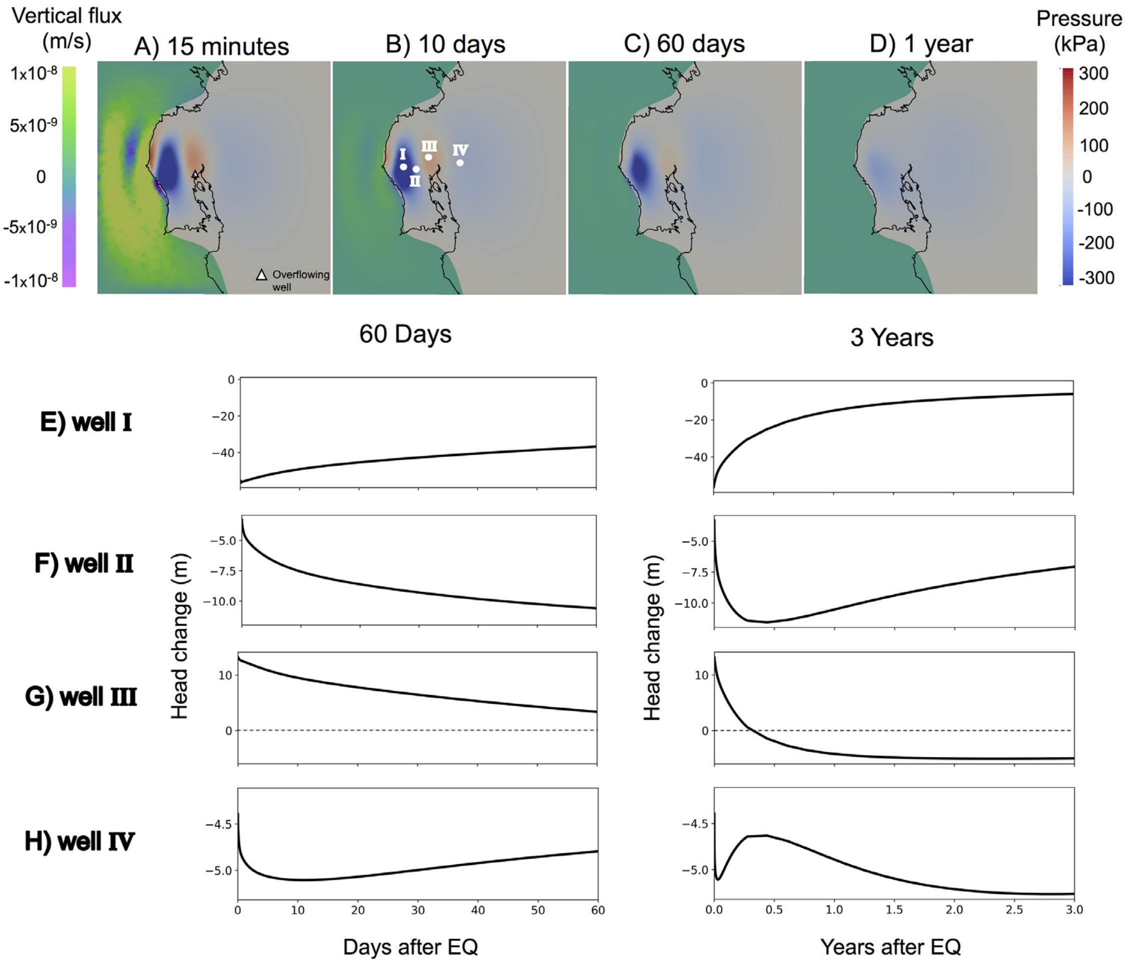

Fig. 10. Three-dimensional model for the 2012 Nicoya earthquake. A-D) Time series showing both the pore pressure in the shallow subsurface on land and the fluid flux through the seabed on composite maps. A groundwater well located at 10.06333N, 85.26055W, which overflowed for several minutes after the earthquake is shown in panel A. E-H) Evolution of the well head at four locations, indicated in panel B.

the peninsula. This also illustrates that there are significant trench-parallel flows in the 3D model, as opposed to only trench perpendicular flow in the 2D model.

Fig. 10a shows that the spatial pattern of fluid fluxes across the ocean floor in the 3D model is more complex than in 2D. In particular, we observe both positive and negative fluid fluxes across the ocean floor. This is due to the complex horseshoe shaped slip distribution of the earthquake. Similar to the 2D simulation, compression leads to a large region of positive SGD between the main slip patch and the trench. However, the complex slip geometry also leads to a trench-parallel region of seawater intake 15–30 km off the coast. Additionally, pore pressure decrease along the coast on the southern portion of the Nicoya peninsula creates a region of seawater intake that persists for many months after the earthquake. This feature may have resulted in seawater intrusion into coastal aquifers.

The temporal evolution of the net fluid exchange across the seafloor is shown in Fig. 11a. Similar to the 2D case, there is a spike in the simulated SGD immediately following the earthquake. During and immediately after an earthquake, pore water is rapidly driven out of the seafloor at a peak net rate of $3.1\cdot10^7$ m^3/day and remains greater than topographic-driven SGD for almost 2 months (Fig. 11a). In 3D this increased outflow drops off more rapidly than in 2D. In the region of seawater intake, the maximum linear vertical flow velocity is 6.7 cm/day.

The SGD produced by a large earthquake can be compared to both SGD due to topography driven flow and SGD due to the continuous compression of the overriding plate by subduction. Elastic compression due to subduction drives fluid out of the crust and into the ocean through the seafloor at a rate of approximately $4.3\cdot10^4$ m^3/day over the study area. This estimate is a lower bound as it does not account for sediment compaction. Fig. 11b

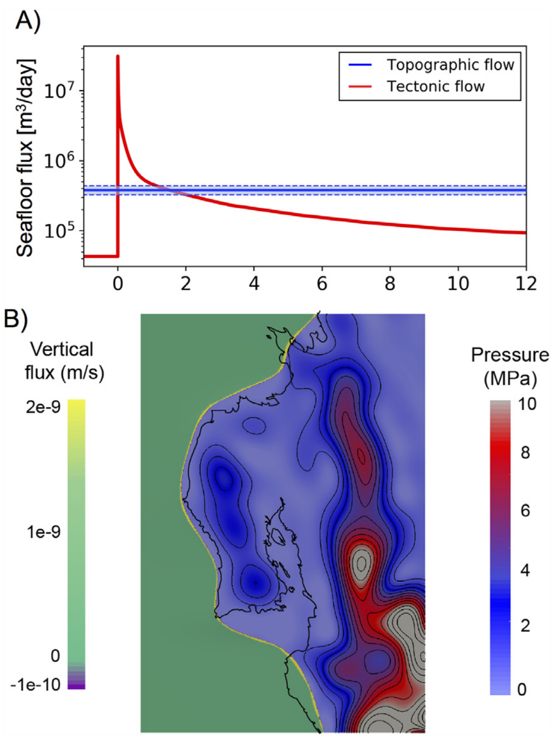

Fig. 11. Comparison of the total SGD produced by topography and tectonic-driven flow in 3D. A) Total flux through the seafloor in 3D before and after the earthquake. The total tectonic SGD remains higher than the topographic SGD for almost 2 months. B) 3D model results for topography driven flow. Surface of 3D model showing vertical fluid velocity offshore and the pressure boundary condition applied on land. This pressure boundary condition is derived from water table height, which is an interpolated as a smooth, subdued expression of topography based on SRTM data (Jarvis et al., 2008). Like in 2D, all of the SGD occurs very close to the coast.

shows the spatial distribution of SGD due to the topography of the Nicoya peninsula. As in 2D the topographically driven SGD occurs in narrow band just offshore and results in the discharge of $3.8{\cdot}10^5$ m^3/day over the study area.The topographic-driven SGD modeled here amounts to less than 1% of the average rainfall received within the study area. Rainfall data was obtained from (https://crudata.uea.ac.uk/cru/data) Harris et al. (2014). In the 30 days after the earthquake, approximately $1.18{\cdot}10^9$ m^3 cubic meters of water are expelled through the seafloor of the model, compared to $1.23{\cdot}10^7$ m^3 attributed to topographic flow. In the 3D simulation, the increase in net SGD due to the earthquake is significant, especially considering the large areas of seawater intake.

4. Discussion

To our knowledge this is the first time a detailed model, incorporating a broad range of data, for the hydrologic response of a large subduction zone earthquake has been assembled. We first discuss our results from the Nicoya Peninsula, followed by a look at the limitations of the available data and the model. Finally, we discuss some future research that may benefit from a combined hydrologic and tectonic approach.

4.1. Timescales of hydrologic response

One of the interesting predictions of the poroelastic model is that the hydrologic response occurs over multiple, distinct timescales. The diffusive relaxation timescale is defined as $t_c = L_c^2/D$, where L_c is the wavelength of the pressure perturbation and $D = \kappa/(\mu S_\epsilon)$ is the hydraulic diffusivity. Different timescales arise because the earthquake causes pressure perturbations with different wavelengths, L_c, and the hydraulic diffusivity decays with depth. This vertical diffusivity variation effectively creates a layered structure comprised of a shallow layer with a high hydraulic diffusivity, $D_u \approx 200$ m^2/s, overlying a lower crust with significantly lower diffusivity, $D_l \approx 8 \cdot 10^{-5}$ m^2/s.

In the shallow layer, the four-lobed instantaneous pressure distribution has two wavelengths of approximately 20 km and 100 km. The relaxation timescale of the shorter wavelength perturbation is approximately 21 days, while the larger wavelength relaxes over approximately one and a half years. The well head evolution in Fig. 10e–h shows these different timescales.

In the lower crust, the characteristic length scale of the instantaneous pressure variation is approximately the rupture length of the earthquake, 40 km. Given the assumed low hydraulic diffusivity in the lower crust, the earthquake induced pressure perturbation decays on the order of 1 Ma, and may explain the persistence of overpressured regions in the lower crust that have been observed seismically (Chaves and Schwartz, 2016). Therefore, while poroelastic variations in the shallow crust decay in the weeks to years after an event, pore pressure changes in the lower crust may persist and interact over many earthquake cycles. Pore pressure changes near the subduction zone interface may also help provide a mechanistic link between slow slip events - both magnitude and spatial distribution - and the main rupture both before (Dixon et al., 2014), and after the earthquake (Voss et al., 2017).

4.2. Limitations

The assumption of linear poroelastic behavior means the model does not capture the effects of dynamic stress changes and other processes, such as consolidation, which occur during and immediately after an earthquake. In the very shallow subsurface (less than 50 m of depth) where there is unconsolidated sediment, these processes may dominate the response of pore pressure to an earthquake.

The appropriate pressure boundary condition for the land surface is not clear. In all of the simulations shown here, except for the case of topographic flow, we have assumed a no flow boundary condition. This boundary condition is appropriate in areas where the head drops, but not where the head rises above the topography. In those locations, groundwater should discharge onto the surface and the head should equal the topographic elevation. However, since it is not known a priori where the induced head change will exceed the land surface elevation, this is a non-linear boundary condition that requires an iterative solution.

Changes in the near surface permeability due to an earthquake have been observed and can be as large as an order of magnitude (Manga et al., 2012; Rojstaczer et al., 1995). However, they have been neglected in this model due to the lack of data constraints.

Similarly, the permeability in the lower crust close to the earthquake may increase due to fracturing as a result of induced pore pressure changes, reducing the time for poroelastic relaxation. Additionally, on the relaxation timescales of the lower crust, viscoelastic relaxation may contribute to deformation and pressure changes.

4.3. Effect on post-seismic deformation

In the weeks and years following the earthquake, continuous surface deformation was observed with GPS monitoring (Malservisi et al., 2015). This post-seismic deformation may be due to after-slip on the fault plane, viscoelastic relaxation of the underlying crust and mantle, and poroelastic deformation in the shallow crust. In order to reliably infer the continued slip on the fault plane, it is necessary to remove the viscoelastic and poroelastic contributions from the surface deformation signal. In general, shorter timescales on the order of days to several weeks are associated with poroelastic effects, while longer timescales on the order of months to years are associated with viscous relaxation (Fialko, 2004; Hetland and Hager, 2006; Jonsson et al., 2003). After-slip may occurs on timescales that overlap with both poro- and viscoelastic relaxation (Helmstetter and Shaw, 2009; Perfettini and Avouac, 2004; 2007). However, this study shows that post-seismic poroelastic deformation can occur on multiple timescales and overlap with those currently linked to viscous relaxation. Attributing surface deformation to these different processes may therefore be more complicated than previously thought. In particular, the non-monotonicity of the poroelastic response may create surface deformation that can be confused with additional slip on the fault interface. It would therefore be useful if surface deformation networks could be complimented by well monitoring to provide additional constraints on the poroelastic component.

5. Conclusion

We have modeled the complex dynamics of the quasi-static poroelastic response to a large subduction zone earthquake and outlined broad hydrologic responses that arise solely due to static stress changes and poroelastic coupling. For the 2012 Nicoya event considered here, the small extent of the slip area relative to the depth of the epicenter leads to a four-lobed instantaneous pressure distribution and subsequent hydrological response. This leads to complex groundwater flow patterns, non-monotonic variations in well head, and poroelastic relaxation on multiple time scales. The model also predicts significant tectonically driven submarine groundwater discharge. In the weeks following the earthquake the tectonic discharge exceeds that due to topography driven flow and occurs farther off-shore. The hydrological response on land is more complex than typically acknowledged in tectonic studies and complicates the interpretation of transient post-seismic surface deformations. Combined tectonic-hydrological observation networks have the potential to reduce such ambiguities.

Acknowledgments

K.A.M. was supported by the National Science Foundation Graduate Research Fellowship under Grant No. DGE-1110007. M.A.H. was supported by NSF grant CBET CDS&E-1508713. This work has benefited from the data and insights provided by Tim Dixon, Rocco Malservisi and the entire Geodesy Lab at the University of South Florida as well as from the mathematical and computational expertise of Omar Ghattas and Umberto Villa at the Institute for Computational Engineering and Science at the University of Texas at Austin. Well data was provided by Carlos Romero at SENARA (National Service of Groundwater, Irrigation and Drainage in Costa Rica) as well as Marino Protti.

The models used here were built using both FEniCS (Alnæs et al., 2014; Logg et al., 2012; Logg and Wells, 2010) and Firedrake (Luporini et al., 2017; Rathgeber et al., 2016) - both collection of open source software components directed at the automated solution of differential equations by finite element method (Balay et al., 2017a; 2017b). Both 2D and 3D meshes were built using GMSH software (Geuzaine and Remacle, 2009). The Generic Mapping Tools software was used to generate figures (Wessel and Smith, 1998).

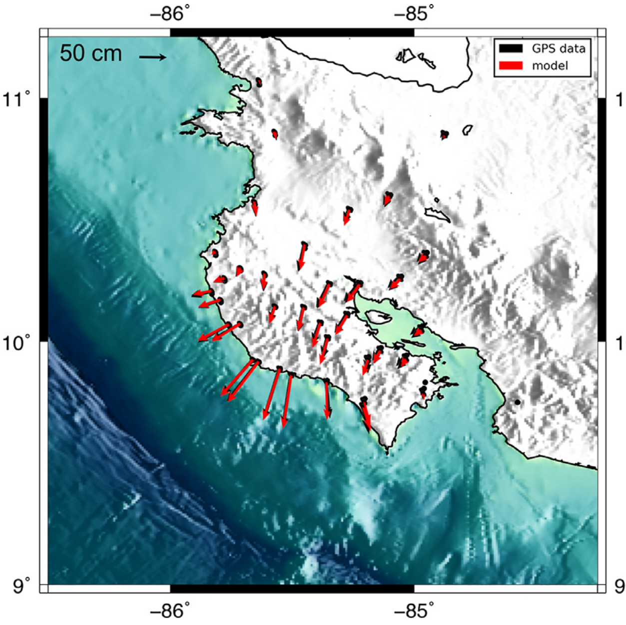

Fig. A.1. Horizontal surface displacements at GPS station locations. Black arrows represent measured co-seismic displacements and red arrows are the initial displacements of the forward model with the inverted-for slip boundary condition. (For interpretation of the references to colour in this figure legend, the reader is referred to the web version of this article.)

Appendix A. Boundary conditions and constitutive equations

The boundary and initial conditions are:

$$p(\cdot,0) = p_0 \qquad \text{in } \Omega \qquad (6a)$$

$$p = 0 \qquad \text{on } \Gamma_{ocean} \qquad (6b)$$

$$(\kappa/\mu\nabla p)\cdot\boldsymbol{n} = 0 \qquad \text{on } \Gamma_{notocean} \qquad (6c)$$

$$\boldsymbol{\sigma}(\boldsymbol{u})\boldsymbol{n} = 0 \qquad \text{on } \Gamma_{surface} \qquad (6d)$$

$$\boldsymbol{u}\cdot\boldsymbol{n} = 0 \qquad \text{on } \Gamma_{right}, \Gamma_{bottom} \qquad (6e)$$

$$\boldsymbol{u}\cdot\boldsymbol{n} = 0 \qquad \text{on } \Gamma_{slab} \qquad (6f)$$

$$\delta\boldsymbol{\sigma}(\boldsymbol{u})\boldsymbol{n}\cdot\boldsymbol{t} + \boldsymbol{u}\cdot\boldsymbol{t} = \boldsymbol{u}_0 \qquad \text{on } \Gamma_{slab} \qquad (6g)$$

The finite element method is a numerical technique to calculate approximate solutions to boundary value problems governed by partial differential equations (PDE's). It uses the variational form of the equation(s) to approximate the solution on a finite number of nodes within the domain. To solve this boundary value problem for fault slip, we need to define stress ($\boldsymbol{\sigma}$) in terms of displacement (u). We use their relationship with the strain tensor to do this. The elastic stress tensor is defined as

$$\boldsymbol{\sigma}(\boldsymbol{\epsilon}) = 2G\boldsymbol{\epsilon} + G\frac{2\nu}{1-2\nu}tr(\boldsymbol{\epsilon})\boldsymbol{I} \qquad (7)$$

The elastic strain tensor in terms of displacement is

$$\boldsymbol{\epsilon}(u) = \frac{1}{2}\left(\nabla\boldsymbol{u} + \nabla\boldsymbol{u}^T\right) \qquad (8)$$

Thus, defining stress only as a function of displacement gives us

$$\boldsymbol{\sigma}(\boldsymbol{u}) = G\left(\nabla\boldsymbol{u} + \nabla\boldsymbol{u}^T\right) + G\frac{2\nu}{1-2\nu}(\nabla\cdot\boldsymbol{u}) \qquad (9)$$

where G and ν are the shear modulus and Poisson's ratio, respectively.

In the FEniCS/Firedrake framework, PDE's are written in their weak form. The weak form of the coupled set of poroelastic equations is:

$$\int_\Omega \boldsymbol{v}\cdot[-\nabla\cdot(\boldsymbol{\sigma}-\alpha p\boldsymbol{I})]\,dx = 0 \tag{10a}$$

$$\int_\Omega q\left[(S_\epsilon p+\alpha\nabla\cdot\boldsymbol{u})_t-\nabla\cdot\left(\frac{\kappa}{\mu}\nabla p\right)\right]dx=0 \tag{10b}$$

Applying Green's identity and solving (6g) for σn gives us the following formulation. Here we find $\boldsymbol{u}\in\boldsymbol{V} := \{\boldsymbol{u}\in\boldsymbol{H}^1(\Omega) : \boldsymbol{u}=0$ on $\Gamma_D, \boldsymbol{u}\cdot\boldsymbol{n}=0$ on $\Gamma_{bottom}\}$ and $\boldsymbol{p}\in\boldsymbol{Q} := \{\boldsymbol{p}\in\boldsymbol{H}^1(\Omega) : \boldsymbol{p}=0$ on $\Gamma_{ocean}\}$ such that:

$$\int_\Omega \boldsymbol{\sigma}(\boldsymbol{u}) : \nabla\boldsymbol{v}-\alpha(\nabla\cdot\boldsymbol{v})p\,dx + \int_{\Gamma_b}\delta^{-1}(\boldsymbol{u}\cdot\boldsymbol{t}-\boldsymbol{u}_0)\boldsymbol{v}\cdot\boldsymbol{t}\,dx = 0 \tag{11a}$$

$$\int_\Omega (S_\epsilon p\,q+\alpha(\nabla\cdot\boldsymbol{u})q)_t+\frac{\kappa}{\mu}\nabla p\cdot\nabla q\,dx + \int_{\Gamma_N}\frac{\kappa}{\mu}(\nabla p\cdot\boldsymbol{n})q\,dx = 0 \tag{11b}$$

The second term in (11a) is the weakly imposed slip boundary condition representing the earthquake slip that occurs within the plane of the slab interface. The second term in (11b) represents imposed boundary flow. For the time-dependent terms, we apply an implicit finite difference time stepping scheme. (11a) has no time derivative and remains the same while (11b) becomes:

$$\int_\Omega S_\epsilon p^k q+\alpha(\nabla\cdot\boldsymbol{u}^k)\,q+\left(\frac{\kappa}{\mu\,dt}\right)\nabla p^k\cdot\nabla q\,dx = \int_\Omega \boldsymbol{S}_\epsilon p^{k-1}\,q+\alpha(\nabla\cdot\boldsymbol{u}^{k-1})\,q\,dx \tag{12}$$

where k is the time level. The timestep becomes larger as the model runs to efficiently capture both rapidly changing early-time behavior and slow late-time behavior. To capture both rapid and slow post-seismic processes, we use timesteps of 15 min for one day, 4 h for 20 days, 2 days for 30 days and 30 days for 10 years in succession.

References

Akita, F., Matsumoto, N., 2004. Hydrological responses induced by the Tokachi-oki earthquake in 2003 at hot spring wells in Hokkaido, Japan. Geophys. Res. Lett. 31 (16), L16603. https://doi.org/10.1029/2004GL020433.

Alnæs, M.S., Logg, A., Ølgaard, K.B., Rognes, M.E., Wells, G.N., 2014. Unified form language: a domain-specific language for weak formulations of partial differential equations. ACM Trans. Math. Softw. 40 (2). https://doi.org/10.1145/2566630.

Balay, S., Abhyankar, S., Adams, M.F., Brown, J., Brune, P., Buschelman, K., Dalcin, L., Eijkhout, V., Gropp, W.D., Kaushik, D., Knepley, M.G., May, D.A., McInnes, L.C., Rupp, K., Sanan, P., Smith, B.F., Zampini, S., Zhang, H., Zhang, H., 2017a. PETSc Users Manual. Technical Report. Argonne National Laboratory.

Balay, S., Abhyankar, S., Adams, M. F., Brown, J., Brune, P., Buschelman, K., Dalcin, L., Eijkhout, V., Gropp, W. D., Kaushik, D., Knepley, M. G., May, D. A., McInnes, L. C., Rupp, K., Smith, B. F., Zampini, S., Zhang, H., Zhang, H., 2017b. PETSc Web page. http://www.mcs.anl.gov/petsc.

Becker, K., Davis, E.E., 2004. In situ determinations of the permeability of the igneous oceanic crust. Hydrogeol. Oceanic Lithosphere 189–224.

Brodsky, E.E., 2003. A mechanism for sustained groundwater pressure changes induced by distant earthquakes. J. Geophys. Res. 108, November 1993, 1–10. https://doi.org/10.1029/2002JB002321.

Chaves, E.J., Schwartz, S.Y., 2016. Monitoring transient changes within overpressured regions of subduction zones using ambient seismic noise. Sci. Adv. 2 (1), e1501289. https://doi.org/10.1126/sciadv.1501289.

Cherry, J., Freeze, A., 1979. Groundwater, 1st Prentice Hall.

Davis, E.E., Villinger, H.W., 2006. Transient formation fluid pressures and temperatures in the Costa Rica forearc prism and subducting oceanic basement: CORK monitoring at ODP Sites 1253 and 1255. Earth Planet. Sci. Lett. 245 (1–2), 232–244. https://doi.org/10.1016/j.epsl.2006.02.042.

DeMets, C., Gordon, R.G., Argus, D.F., 2010. Geologically current plate motions. Geophys. J. Int. 181, 1–80. https://doi.org/10.1111/j.1365-246X.2009.04491.x.

DeShon, H.R., 2004. Evidence for serpentinization of the forearc mantle wedge along the Nicoya Peninsula, Costa Rica. Geophys. Res. Lett. 31 (21), L21611. https://doi.org/10.1029/2004GL021179.

DeShon, H.R., Schwartz, S.Y., Newman, A.V., González, V., Protti, M., Dorman, L.M., Dixon, T.H., Sampson, D.E., Flueh, E.R., 2006. Seismogenic zone structure beneath the Nicoya Peninsula, Costa Rica, from three-dimensional local earthquake P - and S -wave tomography. Geophys. J. Int. 164 (1), 109–124. https://doi.org/10.1111/j.1365-246X.2005.02809.x.

Dixon, T.H., Jiang, Y., Malservisi, R., McCaffrey, R., Voss, N., Protti, M., Gonzalez, V., 2014. Earthquake and tsunami forecasts: relation of slow slip events to subsequent earthquake rupture. Proc. Natl. Acad. Sci. 111 (48), 17039–17044 arXiv:1408.1149, doi:10.1073/pnas.1412299111.

Feng, L., Newman, A.V., Protti, M., González, V., Jiang, Y., Dixon, T.H., 2012. Active deformation near the Nicoya Peninsula, northwestern Costa Rica, between 1996 and 2010: Interseismic megathrust coupling. J. Geophys. Res. 117 (B6), B06407. https://doi.org/10.1029/2012JB009230.

Fialko, Y., 2004. Evidence of fluid-filled upper crust from observations of postseismic deformation due to the 1992 7.3 Landers earthquake. J. Geophys. Res. 109 (B8). https://doi.org/10.1029/2004JB002985.

Geuzaine, C., Remacle, J.-F., 2009. Gmsh: a 3-d finite element mesh generator with built-in pre-and post-processing facilities. Int. J. Numer. Methods Eng. 79 (11), 1309–1331.

Gleeson, T., Befus, K.M., Jasechko, S., Luijendijk, E., Cardenas, M.B., 2015. The global volume and distribution of moderngroundwater. Nat. Geosci. 9 (2), 161–167. https://doi.org/10.1038/ngeo2590.

Harris, I., Jones, P., Osborn, T., Lister, D., 2014. Updated high-resolution grids of monthly climatic observations the cru ts3.10 dataset. Int. J. Climatol. 34 (3), 623–642. https://doi.org/10.1002/joc.3711.

Helmstetter, A., Shaw, B.E., 2009. Afterslip and aftershocks in the rate-and-state friction law. J. Geophys. Res. 114 (B1).

Hetland, E.A., Hager, B.H., 2006. The effects of rheological layering on postseismic deformation. Geophys. J. Int. 166 (1), 277. https://doi.org/10.1111/j.1365-246X.2006.02974.x. /oup/backfile/content_public/journal/gji/166/1/10.1111/j.1365-246x.2006.02974.x/3/166-1-277.pdf.

Jarvis, A., Reuter, H. I., Nelson, A., Guevara, E., et al., 2008. Hole-filled srtm for the globe version 4. available from the CGIAR-CSI SRTM 90m Database (http://srtm.csi.cgiar.org).

Jiang, Y., Liu, Z., Davis, E.E., Schwartz, S.Y., Dixon, T.H., Voss, N., Malservisi, R., Protti, M., 2017. Strain release at the trench during shallow slow slip: the example of Nicoya Peninsula, Costa Rica. Geophys. Res. Lett. 44 (10), 4846–4854. https://doi.org/10.1002/2017GL072803.

Jonsson, S., Segall, P., Pedersen, R., Grimur, B., 2003. Post-earthquake ground movements correlated to pore-pressure transients. Nature 424 (July), 179–183. doi:10.1038/nature01758.1

Kuang, X., Jiao, J.J., 2014. An integrated permeability-depth model for earth's crust. Geophys. Res. Lett. 41 (21), 7539–7545. 2014GL061999, doi: 10.1002/2014GL061999.

Labonte, A.L., Brown, K.M., Fialko, Y., 2009. Hydrologic detection and finite element modeling of a slow slip event in the Costa Rica prism toe. J. Geophys. Res. 114 (December 2008), 1–13. https://doi.org/10.1029/2008JB005806.

Logg, A., Mardal, K.-A., Wells, G.N., et al., 2012. Automated Solution of Differential Equations by the Finite Element Method. Springer. https://doi.org/10.1007/978-3-642-23099-8.

Logg, A., Wells, G.N., 2010. Dolfin: automated finite element computing. ACM Trans. Math. Softw. 37 (2). https://doi.org/10.1145/1731022.1731030.

Luporini, F., Ham, D.A., Kelly, P.H.J., 2017. An algorithm for the optimization of finite element integration loops. ACM Trans. Math. Softw. 44, 3:1–3:26. https://doi.org/10.1145/3054944. 1604.05872.

Malservisi, R., Schwartz, S.Y., Voss, N., Protti, M., Gonzalez, V., Dixon, T.H., Jiang, Y., Newman, A.V., Richardson, J., Walter, J.I., Voyenko, D., 2015. Multiscale postseismic behavior on a megathrust: the 2012 Nicoya earthquake, costa rica. Geochem. Geophys. Geosyst. 16 (6), 1848–1864. https://doi.org/10.1002/2015GC005794.

Manga, M., Beresnev, I., Brodsky, E.E., Elkhoury, J.E., Elsworth, D., Ingebritsen, S.E., Mays, D.C., Wang, C.-Y., 2012. Changes in permeability caused by transient stresses: field observations, experiments, and mechanisms. Rev. Geophys. 50 (2). https://doi.org/10.1029/2011RG000382.

Manga, M., Wang, C.Y., 2007. Earthquake hydrology. In: Treatise on Geophysics, 4. Elsevier, pp. 293–320. https://doi.org/10.1016/B978-044452748-6.00074-2.

Masterlark, T., Demets, C., Wang, H.F., Sanchez, O., Stock, M.J., 2001. Homogeneous vs heterogeneous subduction zone models' Coseismic and postseismic deformation. Geophys. Res. Lett. 28 (1), 4047–4050. https://doi.org/10.1029/2001GL013612.

Miller, S.A., 2012. Shaken and stirred: chilling the crust with earthquakes. Geology 40, 191–192. https://doi.org/10.1016/j.epsl.

Mohr, C.H., Manga, M., Wang, C.-Y., Korup, O., 2016. Regional changes in streamflow after a megathrust earthquake. Earth Planet. Sci. Lett. 123111 (8), 301–311. https://doi.org/10.1016/j.epsl.2016.11.013.

Moore, W.S., 1996. Large groundwater inputs to coastal waters revealed by 226ra enrichments. Nature 380 (6575), 612.

Murphy, B.S., 2014. PyKrige: Development of a Kriging Toolkit for Python. AGU Fall Meeting. H51K-0753.

Peltzer, G., Rosen, P., Rogez, F., Hudnut, K., 1998. Poroelastic rebound along the Landers 1992 earthquake surface rupture. J. Geophys. Res. 103 (98), 30131. https://doi.org/10.1029/98JB02302.

Perfettini, H., Avouac, J.-P., 2004. Postseismic relaxation driven by brittle creep: a possible mechanism to reconcile geodetic measurements and the decay rate of aftershocks, application to the chi-Chi earthquake, taiwan. J. Geophys. Res. 109 (B2).

Perfettini, H., Avouac, J.-P., 2007. Modeling afterslip and aftershocks following the 1992 landers earthquake. J. Geophys. Res. 112 (B7).

Protti, M., 2015. Personal communication.

Protti, M., González, V., Newman, A.V., Dixon, T.H., Schwartz, S.Y., Marshall, J.S., Feng, L., Walter, J.I., Malservisi, R., Owen, S.E., 2013. Nicoya earthquake rupture anticipated by geodetic measurement of the locked plate interface. Nat. Geosci. 7 (2), 117–121. https://doi.org/10.1038/ngeo2038.

Quilty, E.G., Roeloffs, E.A., 1997. Water-Level changes in response to the 20 december 1994 earthquake near parkfield, California. Bull. Seismol. Soc. Am. 87 (2), 310–317.

Rathgeber, F., Ham, D.A., Mitchell, L., Lange, M., Luporini, F., McRae, A.T.T., Bercea, G.-T., Markall, G.R., Kelly, P.H.J., 2016. Firedrake: automating the finite element method by composing abstractions. ACM Trans. Math. Softw. 43 (3), 24:1–24:27. https://doi.org/10.1145/2998441. 1501.01809.

Rojstaczer, S., Wolf, S., Manga, M., 1995. Permeability enhancement in the shallow crust as a cause of earthquake-induced hydrological changes. Nature 237–239.

Sawyer, A.H., David, C.H., Famiglietti, J.S., 2016. Continental patterns of submarine groundwater discharge reveal coastal vulnerabilities. Science 353 (6300), 705–707. https://doi.org/10.1126/science.aag1058.

Schruben, P. G., 1996. Geology and resource assessment of costa rica at 1:500,000 scale – a digital representation of maps of the u.s. geological survey's 1987 folio i-1865. https://pubs.usgs.gov/dds/dds19/.

Screaton, E.J., Saffer, D.M., 2005. Fluid expulsion and overpressure development during initial subduction at the Costa Rica convergent margin. Earth Planet. Sci. Lett. 233 (3–4), 361–374. https://doi.org/10.1016/j.epsl.2005.02.017.

SENARA,. Servicio nacional de aguas subterraneas, riego y avenamiento.

Shi, Z., Wang, G., Liu, C., 2013. Co-Seismic groundwater level changes induced by the may 12, 2008 wenchuan earthquake in the near field. Pure Appl. Geophys. 170 (11), 1773–1783. https://doi.org/10.1007/s00024-012-0606-1.

Shi, Z., Wang, G., Manga, M., Wang, C.-Y., 2015. Continental-scale water-level response to a large earthquake. Geofluids 15 (1–2), 310–320. https://doi.org/10.1111/gfl.12099.

Slomp, C.P., Van Cappellen, P., 2004. Nutrient inputs to the coastal ocean through submarine groundwater discharge: controls and potential impact. J. Hydrol. 295 (1–4), 64–86. https://doi.org/10.1016/j.jhydrol.2004.02.018.

Spinelli, G.A., Giambalvo, E., Fisher, A.T., 2004. Sediment permeability, distribution, and influence on fluxes in oceanic basement. In: Hydrogeol. Ocean. Lithosph. Cambridge University Press., pp. 151–188.

Toth, J., 1962. A theory of groundwater motion in small drainage basins in Central Alberta, Canada. J. Geophys. Res. 67 (11), 4375–4387. https://doi.org/10.1029/JZ067i011p04375.

Voss, N.K., Malservisi, R., Dixon, T.H., Protti, M., 2017. Slow slip events in the early part of the earthquake cycle. J. Geophys. Res. 122 (8), 6773–6786. https://doi.org/10.1002/2016JB013741.

Wakita, H., 1975. Water wells as possible indicators of tectonic strain. Science 189 (4202), 553–555.

Wang, C.Y., Chia, Y., 2008. Mechanism of water level changes during earthquakes: near field versus intermediate field. Geophys. Res. Lett. 35 (12), 1–5. https://doi.org/10.1029/2008GL034227.

Wang, C.-Y., Manga, M., 2010. Hydrologic responses to earthquakes and a general metric. Geofluids 206–216. https://doi.org/10.1111/j.1468-8123.2009.00270.x.

Wang, H., 2000. Theory of Linear Poroelasticity with Applications to Geomechanics and Hydrogeology.

Wessel, P., Smith, W.H., 1998. New, improved version of generic mapping tools released. Eos, Trans. Am. Geophys. Union 79 (47). 579–579

Williams, C.a., Wallace, L.M., 2015. Effects of material property variations on slip estimates for subduction interface slow-slip events. Geophys. Res. Lett. 1–9. https://doi.org/10.1002/2014GL062505.Received.

Yue, H., Lay, T., Schwartz, S.Y., Rivera, L., Protti, M., Dixon, T.H., Owen, S., Newman, A.V., 2013. The 5 september 2012 Nicoya, Costa Rica Mw 7.6 earthquake rupture process from joint inversion of high-rate GPS, strong-motion, and teleseismic P wave data and its relationship to adjacent plate boundary interface properties. J. Geophys. Res. 118 (September 2012), 5453–5466. https://doi.org/10.1002/jgrb.50379.

Zhou, X., Burbey, T.J., 2014. Pore-pressure response to sudden fault slip for three typical faulting regimes. Bull. Seismol. Soc. Am. 104 (2), 793–808. https://doi.org/10.1785/0120130139.